UNIVERSITY OF CALIFORNIA

Santa Barbara

Southern African Monsoon strengthening and weakening of Mozambique Channel through flow during Heinrich events

A Thesis submitted in partial satisfaction of the

requirements for the degree Master of Science

in Earth Science

by

Yue Ma

Committee in charge:

Professor Syee Weldeab, Chair

Professor Lorraine E. Lisiecki

Professor Morgan R. Raven

December 2020

The thesis of Yue Ma is approved.

_____

Lorraine E. Lisiecki

_____

Morgan R. Raven

_____

Syee Weldeab, Committee Chair

September 2020

ACKNOWLEDGEMENTS

This thesis is dedicated to my family for their unconditional love and support. I would especially like to thank my advisor, Professor Syee Weldeab, for the patience he has demonstrated and the time he has dedicated, toward sharpening my thinking and bringing my work to a higher level. I am also grateful for my committee members, Professors Lorraine Lisiecki and Morgan Raven, for their constructive criticism and insightful conversations. I would also like to thank Peter Green and Yann Richard for the support.

ABSTRACT

Southern African Monsoon strengthening and weakening of Mozambique Channel through flow during Heinrich events

by

Yue Ma

The Mozambique Channel is a conduit of trade wind-driven, warm and salty throughflow that is a key component of the Agulhas Current and Agulhas leakage. Agulhas leakage is a flux of warm and salty water from the tropical Indian to the Atlantic Ocean and is thought to strengthen the Atlantic meridional overturning circulation (AMOC). Previous studies from the Agulhas region suggest that enhanced Agulhas leakage, driven by shift and intensification of the southern hemisphere westerlies, played an important role in accelerating glacial terminations. The southeastern monsoon response to freshwater-induced climate instabilities that punctuated the last deglaciation and its impact on the Mozambique Channel through flow and, by extension, on the Agulhas leakage is not well understood. Here we present a high-resolution hydroclimate and mixed layer temperature reconstruction using three sediment cores collected from the runoff-influenced eastern Mozambique Channel, off northwestern Madagascar, in the core region of the southern hemisphere monsoon domain. Local $\delta^{18}O$ seawater time-series, obtained by removing the calcification temperature and ice volume imprints on $\delta^{18}O$ of *Globigerinoides ruber* tests, is used as a proxy of river runoff and, by extension, precipitation changes over

northwestern Madagascar. Superimposed on orbital scale climate trend that indicates a humid glacial, the proxy record reveals precipitation increases centered at 11-13 thousand years before present (kyr BP), 14-18 kyr BP, and 23-25 kyr BP. Considering age model uncertainty, this is the first strong and consistent evidence for southern African monsoon strengthening in response to freshwater forcing during Younger Dryas (YD), Heinrich Event 1 (H1), and Heinrich Event 2 (H2). Furthermore, our study shows a reversal of mixed layer temperature gradient between the west and east Mozambique Channel during H1 and YD. Consistent with the results of climate simulation, we suggest that the gradient reversal indicates a weakening of the trade wind-driven South Equatorial Current and Mozambique Channel throughflow that weakens the Agulhas leakage. In conclusion, the results of this study indicate that millennial scale weakening of Mozambique Channel through flow is strongly linked to the changes in the southern hemisphere monsoon wind fields over the Tropical Indian Ocean. As shown in this study, the latter is sensitive to northern high latitude freshwater forcing, potential creating a positive feedback that contributes to the weakening of the AMOC by reducing the amount of heat and salt leakage into the Atlantic.

TABLE OF CONTENTS

1. Introduction

Oceanic gateways play a key role in interbasin heat and salt exchanges, modulating global ocean circulation and hydrological cycles (von der Heydt and Dijkstra, 2008). The Mozambique Channel is one of the two pathways through which warm and salty tropical Indo-Pacific Ocean water is funneled to the southwestern Indian Ocean to form the Agulhas Current and Agulhas Return Current (Beal et al., 2011; Biastoch et al., 1999; Schott et al., 2009). South of South Africa, a small fraction of tropical Indo-Pacific Ocean water leaks (Agulhas leakage) into the Atlantic Ocean in the form of eddies. Over the last five decades, the Agulhas leakage is increasing in response to a warming climate and, as a result, southward shift of the southern hemisphere westerlies (Beal et al., 2011; Biastoch et al., 2009; Biastoch et al., 2015). In addition to changes in the position and strength of the southern hemisphere westerlies, recent instrumental observation and model simulations reveal that seasonal changes in the monsoon wind fields over the tropical Indian Ocean exert a strong control on the amount of water transport through the Mozambique Channel and, as a result, the Agulhas leakage (Backeberg et al., 2012; Biastoch et al., 1999) (Biastoch et al., 2015). A sustained increase of leakage of salty water into South Atlantic and its advection to North Atlantic is thought to stabilize and strengthen the Atlantic Meridional Overturning Circulation (AMOC) (Backeberg et al., 2012; Biastoch et al., 2015; Biastoch et al., 1999).

On the orbital scale, paleoclimate studies indicate an increase of the Agulhas leakage during deglaciations and suggest that the leakage was caused by a southward shift of the westerlies and contributed to strengthening of the AMOC and, as a result, accelerated the termination of the glacial episodes (Beal et al., 2011; Caley et al., 2012; Franzese et al., 2006; Peeters et al., 2004; Simon et al., 2013). Most of these studies are based on marine sediments around the region of Agulhas Current and assume a direct link between changes in the strength of the Agulhas Current and Agulhas leakage (Caley et al., 2012; Marino et al., 2013; Martinez-Mendez et al., 2010; Simon et al., 2013) with the exception of the study by Peeters et al. (2004) that is centered on the Atlantic sector and most likely records faunal signatures linked to changes in the Agulhas leakages (Figure 1). Furthermore, the relatively low resolution of the existing records does not allow detail examinations of the response of the Agulhas leakage to millennial-scale climate perturbations such as the Heinrich events. More importantly, past changes in the water mass transport through the Mozambique Channel and their potential association with changes in trade winds have, to our knowledge, not been considered, despite being critical for an improved understanding of tropical influence on the Agulhas leakage. In particular, the response of the

southeastern African monsoon to the deglacial fresh water forcings and the impact on the monsoonal wind-driven water mass transport through the Madagascar Channel has not been explored yet. The limited numbers of paleoclimate studies focusing on southeastern African monsoon draw a complex and spatially heterogeneous pattern, often with conflicting results and interpretation (Khon et al., 2014; Schefuß et al., 2011; Scroxton et al., 2019; Wang et al., 2013a; Wang et al., 2013b; Weldeab et al., 2014; Williamson et al., 1998), most likely reflecting regionally heterogeneous response and varying proxy sensitivity. The lack of spatially and temporally coherent hydroclimate records of the region impedes efforts to deducing the dominant forcings and its role in co-shaping global climate changes.

This study extends the spatial and temporal coverage of southeastern African Monsoon reconstruction by focusing on three highly resolved marine sediment cores collected off northwestern Madagascar. The results of this study show for the first time a strong and consistent evidence of southern African monsoon strengthening during meltwater-induced, large-scale atmospheric perturbations during the last deglacial and the last glacial. Based on surface temperature gradient reconstruction within the Mozambique Channel, our record indicates a weaker water mass transport through the channel during the deglaciation, reducing the tropical Indian Ocean's influence on the Agulhas leakage.

2. Settings

2.1 Precipitation

Precipitation over Madagascar is primarily controlled by the southern African monsoon that is a component of the southern hemisphere monsoon system (Figure 1) (Arivelo and Lin, 2016). During austral summer (December-to-March: DJFM), the Inter-Tropical Convergence Zone (ITCZ) shifts southward and brings monsoon rainfall to northwestern Madagascar (Figure 1). Over the Betsiboka, Mahavavy, Mahajamba, and Sofia (BMMS) basin, which is the focus of this study (Figures 1A), DJFM precipitation varies between 250 and 560 mm/month (Figure 2 A). The low elevation region (below 700 m above sea level) within the BMMS basin receives more precipitation (300-560 mm/month) compared to the high elevation (> 1000 m above sea level) that receives 250-to-300 mm/month precipitation during the wet season (Figures 1B and 2B). During austral winter (June to August: JJA), northwestern Madagascar receives monthly precipitation less than 20 mm/month (Figures 1B and 2B). Relatively low-resolution data of annually averaged $\delta^{18}O$ of precipitation over the BMMS river basin show a strong modulation by the topography (Bowen et al., 2005), with $\delta^{18}O$ values between -4.82 ‰ and -5.74 ‰ over the low

elevation (below 700 m above sea level) and -9.38 and -7.56 ‰ over the high elevation region (> 1000 m above sea level) (Figures 2A-D).

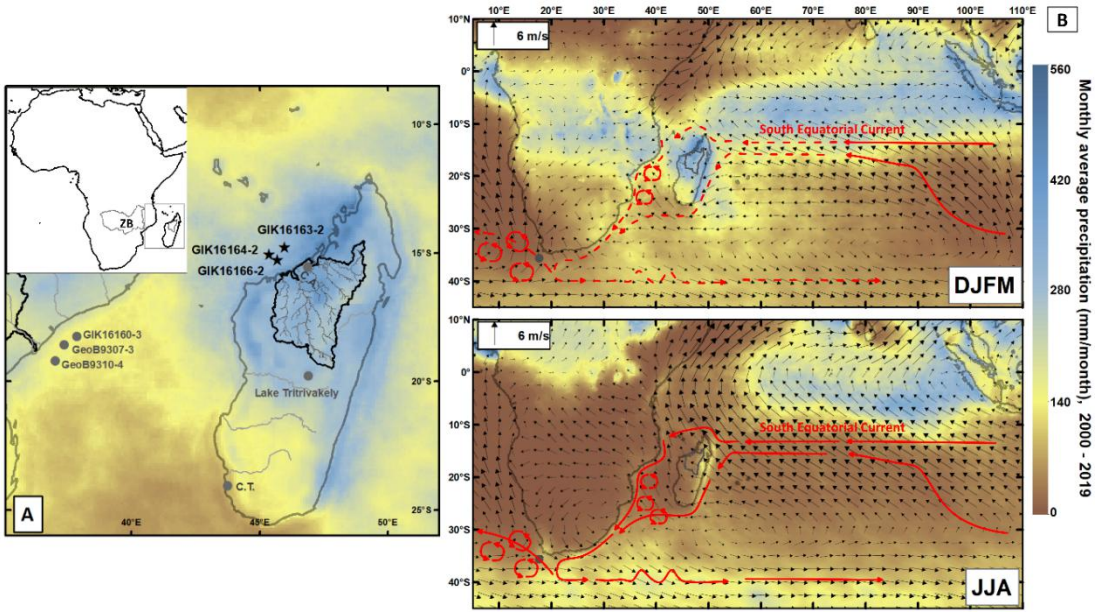

Figure 1: Summer and winter precipitation over the tropical Indian Ocean and adjacent land mass and ocean surface currents. A) View of the study area, showing austral summer precipitation (December-to-March) and location of off Madagascar marine sediment cores used in this study and other relevant study sites. Also indicated is the boundary of the BMMS basin and river networks. Location and extent of Zambezi Basin (ZB) is indicated in the inlet. B) Seasonal precipitation and wind field patterns over the tropical Indian Ocean and adjacent land mass during austral a summer (December-to-March: DJFM) and austral winter (June-to-August: JJA). Red arrows indicate a schematic depiction of relevant ocean surface currents. Dotted lines in Figure 1B (top) indicate weaker current compared to these indicated in Figure 1B (bottom). Data source: Monthly average precipitation and surface winds collected over the time window between 2000 and 2019 (Huffman et al., 2019; Kalnay et al., 1996).

With a combined catchment area of 116,000 km^2, the BMMS basin drains northwestern Madagascar (Figures 1 and 2). During the wet season the Betsiboka River, the largest of the three rivers, has a discharge of 600 to 1600 m^3/s (Marwick et al., 2014). The seasonal runoff of the rivers has noticeable impact on the sea surface salinity (SSS) in the northeastern part of the Mozambique Channel (Figures 2A and 2B). The preservation of this runoff imprint in the surface water of northeastern Mozambique Channel is enhanced due to weak wind and current mixing, resulting in

relatively shallow mixed layer (Figures 2E & F).

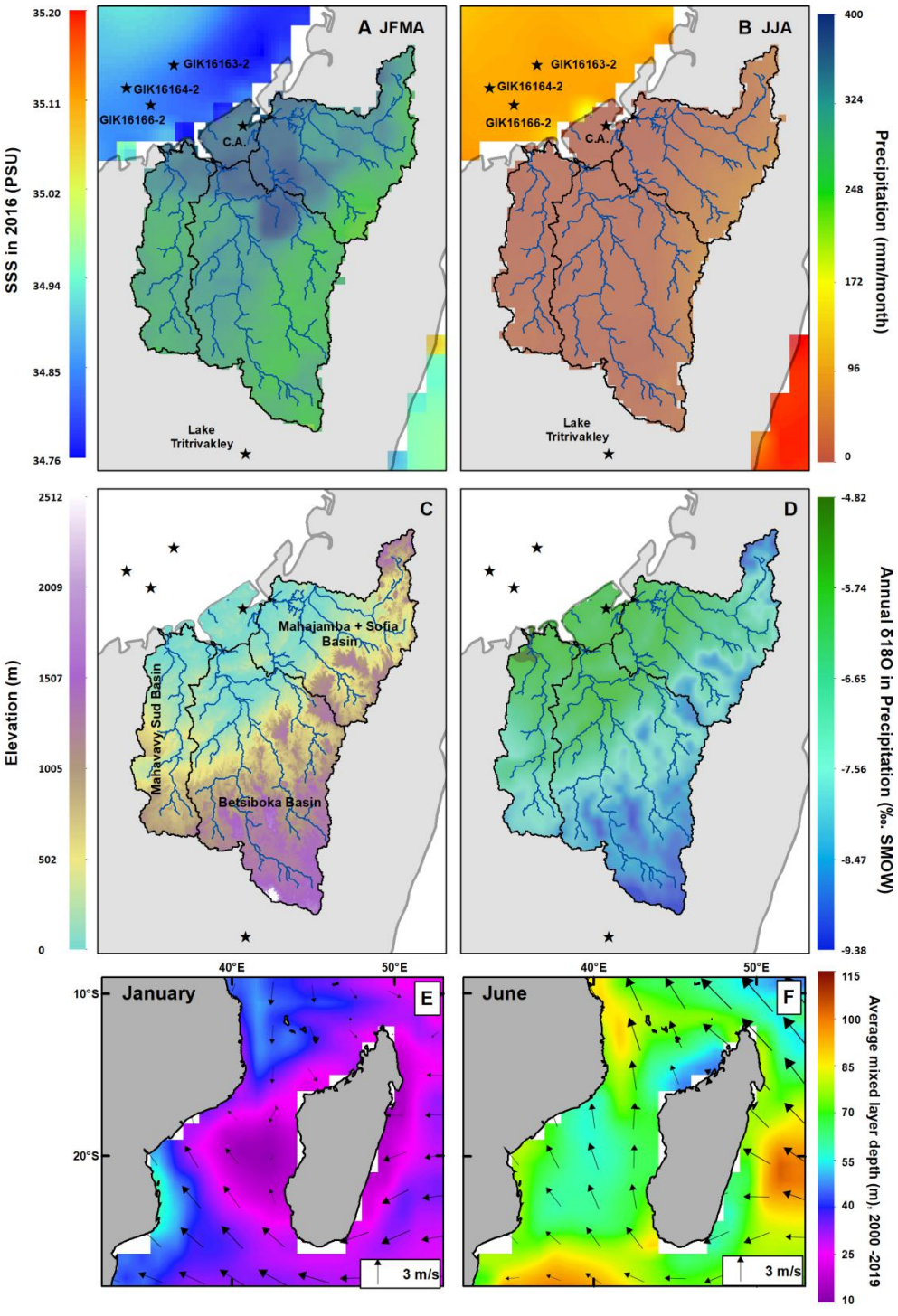

Figure 2: Hydroclimatic and topographic features of the of BMMS basin and its runoff impact on the sea surface salinity (SSS) in northeastern Mozambique Channel. A and B) Monthly average precipitation (2000 to 2019) during wet and dry season over Madagascar (Huffman et al., 2019). Shown is also runoff impact on the SSS over the sediment core

location in 2016 (Wentz et al., 2014). C) Topography of the BMMS basin (U.S. Geological Survey's Center for Earth Resources Observation and Science, 1996). D) Spatial pattern of annually averaged and spatially interpolated $\delta^{18}O$ of precipitation (Bowen et al., 2005). E and F) Mixed layer depth and monthly surface winds in January and June (Behringer and Xue, 2004; Kalnay et al., 1996).

2.2 Mozambique Channel

2.2.1. Seasonal SST pattern

Sea surface temperature within the Mozambique Channel varies seasonally and spatially (Figure 3). Average surface water temperatures are 29-30 C° and 26-27 C° during the austral summer and winter, respectively, and surface water in the eastern part of the Mozambique Channel is warmer than in the western part (Figure 3). The resulting east-west temperature gradient is about 1.2 °C in the north (at 15°S) and weakens to 0.9 °C in the south (at 24°S). Spatial SST variation in the Mozambique Channel occurs due to spatially varying wind fields and southward propagating current and eddies along the Mozambique coastal lines (Backeberg and Reason, 2010; Han et al., 2019; Malauene et al., 2014; Swart et al., 2010). The mountains in eastern Madagascar significantly weaken and divert the easterly winds (Figure 3), leading to a shallower mixed layer depth in eastern Mozambique Channel (Figure 2E-F) and, as a result, elevated SST compared to the western Mozambique Channel (Figure 3). The southward passage of eddies and currents along the African continental margin also contributes to the east-west gradient, though modestly. The anticyclonic and cyclonic eddies have different effects on the SST of the Mozambique Channel. While the anticyclonic eddies raise the SST (Swart et al., 2010), the cyclonic eddies bring relatively cold deep water to the mixed layer (Malauene et al., 2014). Because the anticyclonic eddies are large in scale (300-350 km in diameter), occur often (average 6-7 per year) and have a long lifetime (14-84 days), they have a stronger effect on the SST of Mozambique Channel than the cyclonic eddies (Han et al., 2019). The anticyclonic eddies increase SST in the western Mozambique Channel by up to 0.15 °C (Han et al., 2019) and, as a result, lower the east-west SST gradient slightly. This is negligibly small compared to the wind-induced SST gradient of up to 1.2 °C (Figure 3). Generally, the east-west SST gradient persists throughout the year, though during the austral summer (December-to-February) the gradient is weaker (Figure 3).

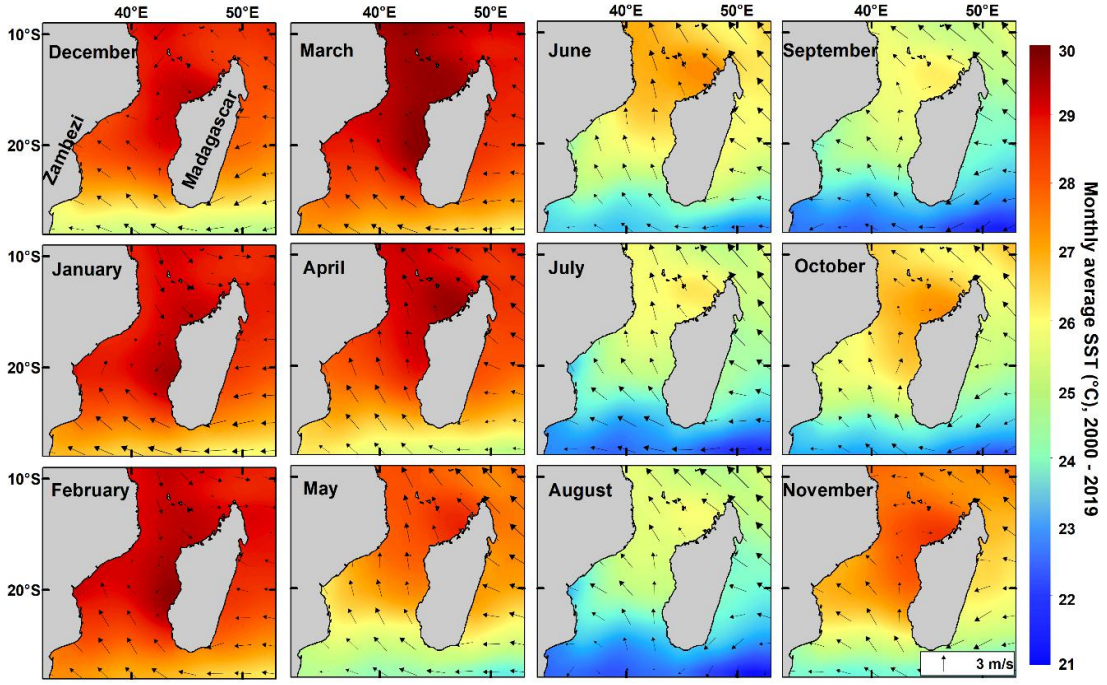

Figure 3: Monthly averaged (2000-2019) sea surface temperature (SST) and direction and strength of wind indicated by arrows (Kalnay et al., 1996). Sea surface temperature data are from (Behringer and Xue, 2004).

2.2.2: Mozambique Channel: a conduit for warm and saline water mass transport

The Mozambique Channel is a conduit for the wind-driven South Equatorial Current and anticyclonic and cyclonic eddies that develop north of the Mozambique Channel and propagate along the western boundary (Backeberg and Reason, 2010; Malauene et al., 2014; Ridderinkhof and de Ruijter, 2003; Ridderinkhof et al., 2010; Swart et al., 2010). The anticyclonic eddies carry, on average, a warm and salty water mass of 16.7±3.1 Sverdrup (Sv:10^6 m^3/second) and feed the Agulhas Current (Backeberg and Reason, 2010; Ridderinkhof and de Ruijter, 2003; Ridderinkhof et al., 2010; Schott et al., 2009; Swart et al., 2010; van der Werf et al., 2010). Seasonal wind fields over the tropical Indian Ocean and associated Ekman transport exerts a strong control on the amount of water mass transport through the Mozambique Channel and East of Madagascar (Backeberg et al., 2012; Biastoch et al., 1999). During austral summer, the Indian Ocean monsoon and the weakening of southeast winds result in a

weak Ekman Transport in both east and west of Madagascar (Figure 1B). During austral winter, the strengthening and continuous southeast winds generate a strong Ekman transport and increase the amount of water mass transport through the Channel (Figure 1B). As the Mozambique through flow joins the Southeast Madagascar Current (Figure 1B), they together form the Agulhas Current (Ridderinkhof and de Ruijter, 2003; Schott et al., 2009; Swart et al., 2010). Southeast of Cape Basin, approximately between 15°E and 20°E, the Agulhas Current returns into the southern Indian Ocean as the Agulhas Return Current (Bryden et al., 2005; Richardson, 2007). Occasionally, the Agulhas Current sheds eddies that leak (Agulhas Leakages) into the Atlantic Ocean. Instrumental observations and ocean-climate simulations demonstrate that on multi-decadal scale, the increase of Agulhas Leakage is linked to warming of Southern Ocean and southward shift southern hemisphere Westerlies and strengthening of Southern Equatorial Current that is driven by the trade winds (Backeberg et al., 2012; Biastoch and Boning, 2013; Biastoch et al., 2008; Biastoch et al., 2009; Biastoch et al., 2015; Biastoch et al., 1999). The warm and salty Agulhas leakages advect to the North Atlantic and are thought to influence the decadal variability of the AMOC (Backeberg et al., 2012; Biastoch et al., 2008; Biastoch et al., 2009; Swart et al., 2010).

3. Material and Methods

3.1 Marine sediment cores and age model

This study focuses on three marine sediment cores that were collected during the Meteor Cruise M75 in 2008 (GIK16163-2: 14°45.47'S, 45°59.20'E, water depth 2579 m; GIK16164-2: 15°30.66'S, 45°22.46'E, water depth 2915 m; and GIK16166-2: 15°16.27'S, 45°41.43'E, water depth 2099 m) (Schneider et al., 2008). To establish an age model for each core, 31 radiocarbon analyses were carried out in tests of mixed-layer dwelling plankton foraminifers (*Globigerinoides ruber* white, *Globigerinoides sacculifer* and *Orbulina universa*) at the Leibniz Laboratory for Radiometric Dating and Stable Isotope Research (University of Kiel, Germany) (Table 1). The ^{14}C-ages were converted to calendar ages using calibration software CALIB version 7.0 (Stuiver et al., 2019) and the Marine13 calibration dataset (Reimer et al., 2013) with a constant reservoir age correction of $\Delta R = 203 \pm 32$ for the Mozambique Channel and adjacent mixed layer water (Southon et al., 2002).

We performed age model analyses using three different approaches (Figure 4): A linear interpolation based on the assumption of a constant sedimentation rate between two adjacent age control points; a Bayesian probabilistic approach using Bacon software (Blaauw and Christen, 2011) with parameters shown in Table 2; and iii) a

relatively new age-depth modeling routine called “Undatable” which includes uncertainty in both age and depth (Lougheed and Obrochta, 2019). Within age model uncertainties that vary between ±200 and ±700 years (2σ), all three age model calculation approaches deliver very similar results (Figure 4). The largest age model uncertainty occurs in GIK16166-2 between 24 and 33 kyr BP, largely falling outside the focus of this study. Four radiocarbon dates in core GIK16163-2 show an age reversal (Figure 4) that we excluded from the final age model calculations used for the

proxy time-series.

Lab Code	Core	Sediment Depth	Sample Material	^{14}C age (yr BP)	Uncertainty ± (yr BP)	Calendar Age Mean	2sigman lower limit (yr BP)	2sigman upper limit (yr BP)
KIA53180	GIK16163-2	0.5	Mixed plk. forams	1847	40	1210	1108	1287
KIA53181	GIK16163-2	10.5	Mixed plk. forams	4328	43	4186	4055	4348
KIA53182	GIK16163-2	25.5	Mixed plk. forams	7350	47	7616	7520	7713
KIA53183	GIK16163-2	40.5	Mixed plk. forams	10460	55	11247	11108	11459
KIA53184	GIK16163-2	50.5	Mixed plk. forams	12470	59	13730	13533	13898
KIA53185	GIK16163-2	61.5	Mixed plk. forams	12300	59	13544	13389	13719
KIA53186	GIK16163-2	71.0	Mixed plk. forams	13585	64	15517	15276	15759
KIA53187	GIK16163-2	90.5	Mixed plk. forams	12720	59	14000	13834	14153
KIA53403	GIK16163-2	104.0	Mixed plk. forams	18840	115	22099	21820	22383
KIA53188	GIK16163-2	115.5	Mixed plk. forams	18850	100	22110	21847	22368
KIA53189	GIK16163-2	149.5	Mixed plk. forams	22540	134	26146	25889	26483
KIA53171	GIK16164-2	1.5	Mixed plk. forams	2218	39	1581	1480	1695
KIA53172	GIK16164-2	10.5	Mixed plk. forams	5660	43	5830	5716	5923
KIA53173	GIK16164-2	20.5	Mixed plk. forams	8120	47	8378	8286	8498
KIA53174	GIK16164-2	30.5	Mixed plk. forams	10755	55	11809	1144	12034
KIA53175	GIK16164-2	44.5	Mixed plk. forams	13445	59	15305	15124	15569
KIA53176	GIK16164-2	56.0	Mixed plk. forams	15295	64	17876	17669	18056
KIA53177	GIK16164-2	65.0	Mixed plk. forams	16325	68	18958	18802	19152
KIA53178	GIK16164-2	85.5	Mixed plk. forams	18875	77	22136	21891	22359
KIA53179	GIK16164-2	98.5	Mixed plk. forams	21060	105	24604	24267	25017
KIA53190	GIK16166-2	4.0	Mixed plk. forams	1245	41	613	534	673
KIA53400	GIK16166-2	16.0	Mixed plk. forams	3715	47	3398	3290	3530
KIA53191	GIK16166-2	37.0	Mixed plk. forams	5920	47	6130	5992	6250
KIA53401	GIK16166-2	55.0	Mixed plk. forams	8675	68	9094	8928	9295
KIA53192	GIK16166-2	76.0	Mixed plk. forams	10145	55	10912	10724	11092
KIA53193	GIK16166-2	100.0	Mixed plk. forams	12250	59	13489	13344	13664
KIA53194	GIK16166-2	151.0	Mixed plk. forams	13045	64	14558	14191	14963
KIA53195	GIK16166-2	185.5	Mixed plk. forams	14285	77	16498	16234	16810
KIA53196	GIK16166-2	215.5	Mixed plk. forams	15670	72	18304	18063	18520
KIA53197	GIK16166-2	361.0	Mixed plk. forams	20085	96	23463	23103	23753
KIA53198	GIK16166-2	544.0	Mixed plk. forams	29190	232	32597	31765	33334

Table 1

31 ^{14}C-dating of monospecific and mixed foraminiferal tests in samples from GIK16163-2, GIK16164-2, and GIK 16166-2. The ^{14}C-ages were converted to calendar ages using calibration software CALIB (version 7.04, Stuiver et al., 2019) and marine13 data set (Reimer et al., 2013) with a constant reservoir age correction $\Delta R = 203 \pm 32$ for Mozambique Channel (Southon et al., 2002).

Core	acc.shape	acc.mean (yr/cm)	mem.strength	mem.mean	sections
GIK16163-2	2	100	80	0.3	76
GIK16164-2	2	200	80	0.5	50
GIK16166-2	1	50	70	0.4	136

Table 2

Parameters used for Bacon Age Model.

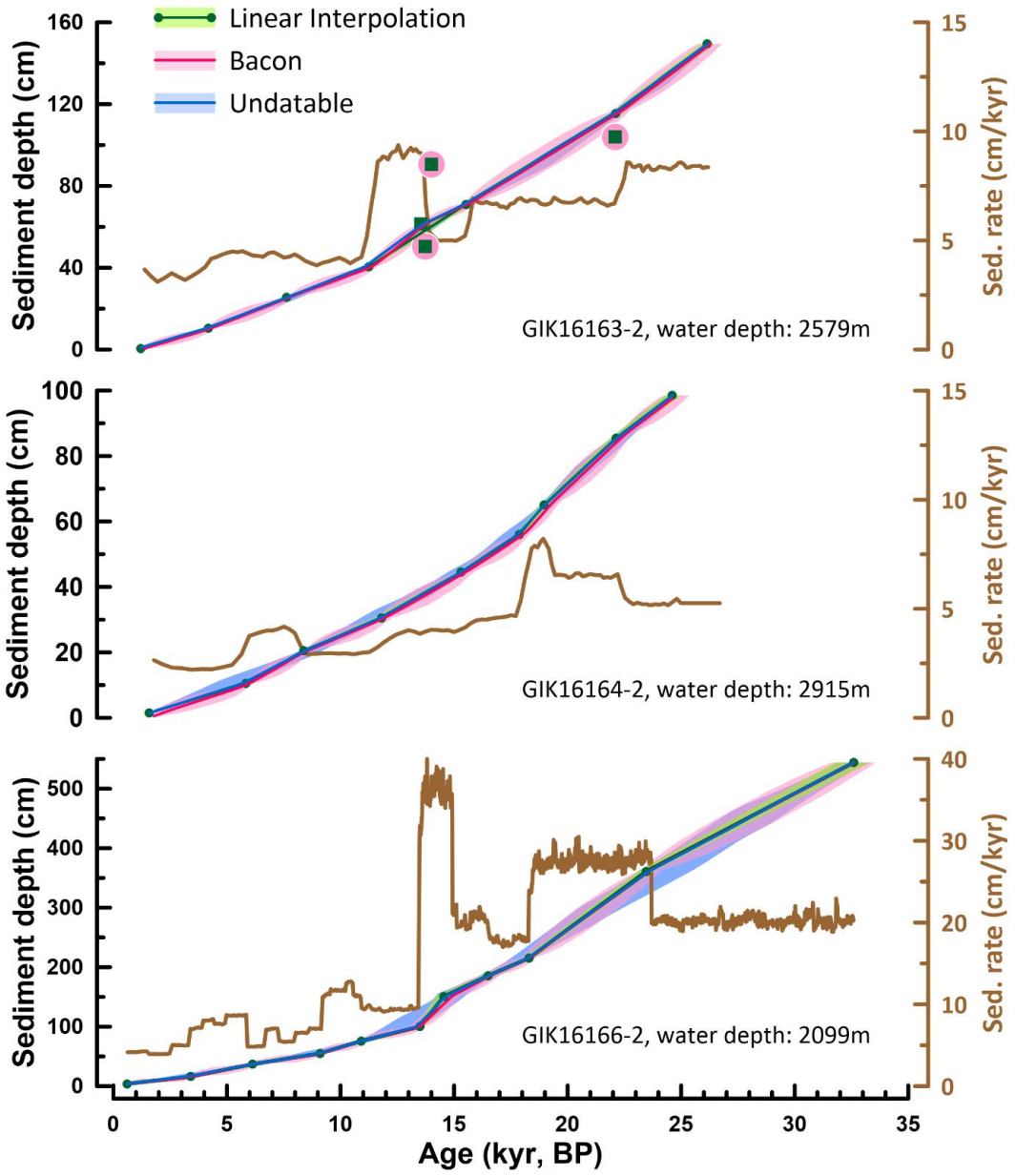

Figure 4: Age models and sedimentation rates of marine sediment cores used in this study: A) GIK16163-2, B) GIK16164-2, and C) GIK 16166-2. Green blue, and red lines indicate age models based on linear interpolation, based on Bacon software (Blaauw and Christen, 2011), and Undatable (Lougheed and Obrochta, 2019), respectively. The envelops indicate 2σ error estimates. Data points indicated by green squares and pink circles were excluded from the linear interpolation and Bacon age models, respectively. Shown is also sediment accumulation rate calculated using the results of the Bacon age models.

3.2 River Mouth - Core Site Distance

To assess the effect of the Holocene-to-glacial sea level change on the distance between the core sites and the river mouth and, as a result, the runoff signal at each core site, we create a sea level-dependent distance profile between the river mouth and core site. We use the bathymetry software GeoMapApp (Ryan et al., 2009) and the well-dated and high resolution eustatic sea level reconstruction of Lambeck et al. (2014). We calculated possible main fresh water pathway scenarios for each core site (Figure 5). The reconstructed pathway is strongly dependent on the sea floor morphology of the estuary that could have been subjected to significant changes during the last Glacial-Holocene transition. As results, the pathway scenarios harbor large uncertainties, and we emphasize that the results of the mouth-core site distance reconstruction should be viewed a semi-quantitative estimate. A common feature to all scenarios is that the major change in the river mouth-core site distance occurred between 8 kyr and 6 kyr BP. Prior to 8 kyr BP, the river mouth-core site distance remained relatively unchanged.

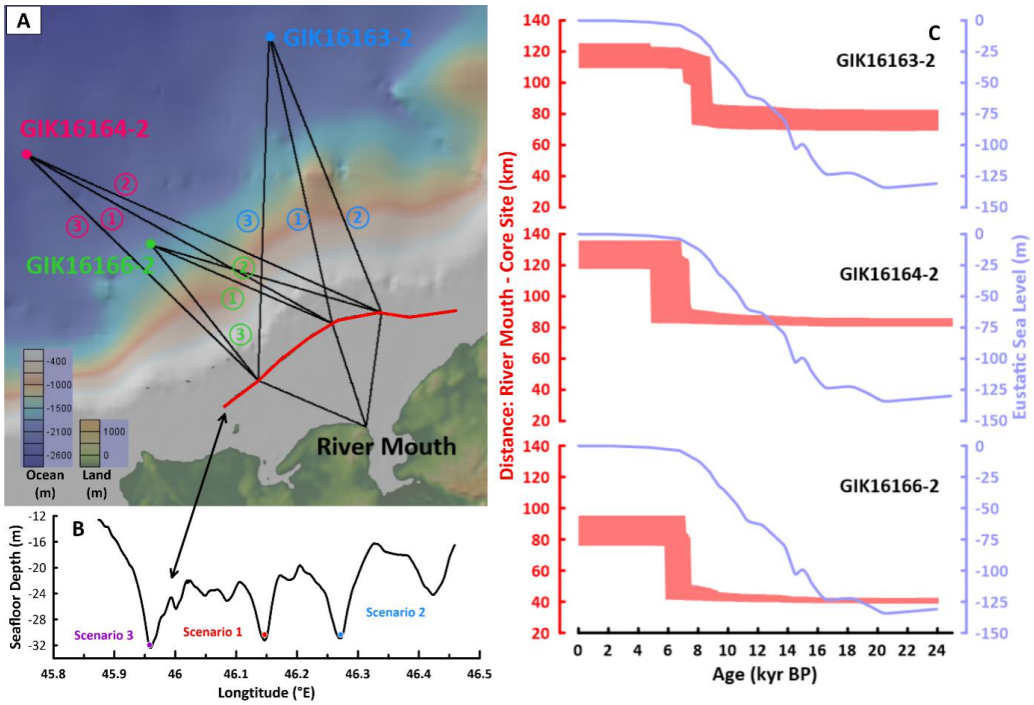

Figure 5: Sea level and pathway dependent river mouth-core site distance estimate. A) Three scenarios of possible runoff pathway to each core site. B) Current estuarine sea floor morphology/bathymetry that may have affected the runoff pathways during the early Holocene and the deglacial sea level rise. C) Result of sea level-dependent river mouth-core site distance. The orange envelope encompasses the difference between the three scenarios. Blue line indicates the eustatic sea level reconstruction of Lambeck et al. (2014).

3.3 Mg/Ca ratio and its conversion to temperature estimates

For the analysis of Mg/Ca in tests of *Globigerinoides ruber* white, in most samples 25-30 individuals of *G. ruber* white (250-300 µm) were selected. The samples were gently crushed into test fragments. Approximately 25 % of the sample were split for the stable isotope analysis. The remaining fraction (~75%) was used for the analysis of Mg/Ca. First, visible grains (silicates, pyrites, Fe-Mn-hydroxides) were removed manually under a stereo microscope using a thin brush hair, followed by both mechanical (sonication in n-pure water and syphoning of the supernatant), oxidative and reductive cleanings as described in Martin and Lea (2002). The reductive step includes sample treatments using a mix of ammonium citrate (~0.25 M)-anhydrous hydrazine-ammonium hydroxide solution (3%) bathed in a boiling water for 30 minutes to remove most of the Mn-Fe-hydroxide coatings and other contaminants. Then the samples were rinsed several times using ultrapure water. The reductive step was followed by the oxidative step to remove organic matters with 3% H_2O_2 buffered by ultrapure sodium hydroxide (1M) in boiling water bath for 10 minutes. After the oxidation step, samples were rinsed several times using ultrapure water. Finally, samples will be dissolved in ultrapure HNO_3 (0.1 M) and Mg/Ca ratios were analyzed using ICP-MS (Element X) at the Institute of Geosciences, University of Kiel (Germany). Accuracy of the data is checked by analyzing the carbonate reference standard ECRM (Greaves et al., 2008) and account for 3.66 % RSD (± 0.08 mmol/mol). Along Mg/Ca we analyzed Al/Ca, Fe/Ca, and Mn/Ca to assess the degree of contaminant removal. The values of Al/Ca, Fe/Ca, and Mn/Ca range 0.017–0.678 µmol/mol, 0.008–0.4390 µmol/mol, 0.011-0.641 µmol/mol, respectively. Samples with high Al/Ca (> 0.7 µmol/mol) that show simultaneously anomalously high Mg/Ca were rejected.

The Mg/Ca time-series is converted into salinity- and pH-corrected estimates of mixed layer temperature estimates. We apply the Mg/Ca-temperature conversion equation of Gray et al. (2018) and Gray and Evans (2019) and use current values of ΔpCO_2 (0 µatm), mixed layer salinity (35.3 PSU), and alkalinity (2313.6 µeq/kg) of the study area (Lee et al., 2006; Locarnini et al., 2013; Zweng et al., 2013). The cumulative error of the SST reconstruction is estimated at ±0.65°C (1σ).

3.4 Oxygen Isotope Composition ($\delta^{18}O$) of foraminiferal calcite and local sea water

We analyzed oxygen isotope ratio ($^{18}O/^{16}O$), expressed as $\delta^{18}O$ (‰, Pee Dee Belemnite (PDB)), in tests of *G. ruber*, a mixed layer dwelling planktonic foraminifer (Schiebel and Hemleben, 2017). The $\delta^{18}O$ analysis was carried out using an MAT253

Stable Isotope Ratio Mass Spectrometer online coupled to Kiel IV at UCSB. The accuracy of the $\delta^{18}O$ analysis was determined by analyzing NBS 19 standards and is ±0.05‰ (2σ). We established a record of calcification temperature- and ice volume-corrected $\delta^{18}O$ of local mixed layer seawater ($\delta^{18}O_{sw}$). To calculate the $\delta^{18}O_{sw}$ time-series, we used the Mg/Ca-based calcification temperature estimate, the temperature – $\delta^{18}O_{calcite}$ – $\delta^{18}O_{seawater}$ equation ($\delta^{18}O_{seawater}$ =[(T-16.5)/4.8+ $\delta^{18}O_{calcite}$ +0.27] (Bemis et al., 1998), and an estimate of $\delta^{18}O_{seawater}$ changes related to secular changes in the ice volume (Lambeck et al., 2014), with a $\delta^{18}O_{seawater}$ change of 0.008±0.001‰ per meter of an eustatic sea level change (Adkins et al., 2002; Spratt and Lisiecki, 2016; Waelbroeck et al., 2002). The error estimate of local $\delta^{18}O_{sw}$ values varies between ±0.190‰ (2σ) for the glacial and deglacial segment and ±0.185‰ for the Holocene record. The cumulative uncertainty is estimated using the following equation: $\sigma = \sqrt{(\sigma T)^2 + (\sigma I)^2 + (\sigma CW)^2 + (\sigma IV)^2 + (\sigma IVU)^2}$, with σT (±0.06‰): uncertainty related to the uncertainty of temperature reconstruction (σ: ±0.65°C), σI (±0.05‰): uncertainty of $\delta^{18}O_{calcite}$ analysis, σCW (±0.168‰): error associated with the calculation of $\delta^{18}O_{seawater}$ using calcification temperature and $\delta^{18}O_{calcite}$, σIV (±0.040‰-to-0‰): uncertainty of reconstruction of global $\delta^{18}O_{seawater}$ changes affected by ice volume uncertainty, and σIVU (± 0.001‰): uncertainty of correcting $\delta^{18}O_{calcite}$ from ice volume.

4. Results

4.1 Sediment accumulation rate

The sedimentation rate in all three cores shows temporal and spatial variation (Figure 4), with glacial and deglacial interval showing relatively high sedimentation rate (5-35 cm/kyr) compared to the Holocene (2-5 cm/kyr). GIK16166-2 whose location is more proximal to the river mouth displays the highest sedimentation rate followed by GIK16163-2 (Figure 4). Common to both cores is an interval of an exceptionally high sedimentation rate centered between 15.5 and 13 kyr BP (37 cm/kyr in GIK16166-2 and 10 cm/kyr in GIK16163-2). The reconstruction of the river mouth-core site distance indicates that changes in sedimentation rate during the glacial, deglacial, and late Holocene are likely associated with changes in the precipitation and erosion rate in the river basin (Figures 4 and 5). Sedimentation rate changes between 5 and 9 kyr BP are correlated with changes in river mouth-core site distance.

4.2 Oxygen isotope composition ($\delta^{18}O$) and Mg/Ca-based temperature estimates

The $\delta^{18}O_{G.\ ruber}$ time-series (Figure 6A), a composite imprint of calcification temperature, global ice volume and local $\delta^{18}O$ seawater changes, shows very similar pattern in all three cores, with relatively enriched isotope compositions (-0.5‰ to -1‰) and relatively depleted compositions (from -2 to -2.5 ‰) during the Holocene and glacial, bridged by a gradual decrease during the deglaciation and the early Holocene (17 - 9 kyr BP). Superimposed on this gradual deglacial change, a relatively abrupt decline in $\delta^{18}O_{G.\ ruber}$ is evident during Heinrich event 1 (H1) and Younger Dryas (YD) in all cores, though the magnitude and timing of changes vary between the cores most likely due to difference in river mouth-core site distance and age model uncertainties, respectively.

Mg/Ca data show an increasing trend from about 3.25 µmol/mol during the glacial period to about 4.25 µmol/mol during the Holocene (Figure 6B). The individual record shows high frequency variability, some of which is present in all cores. In some segments, the resolution of Mg/Ca time-series is lower than the $\delta^{18}O_{G.\ ruber}$ record due low foraminifer abundance, sample loss during cleaning, and removal of data points with elevated silicate phases, as indicated by high Al/Ca values. Because the core sites are closely located to each other, we assume that the spatial difference of mixed layer temperature, if any, in the past was significantly smaller than the uncertainty of SST reconstruction (±0.65°C). Hence, using the Mg/Ca data of all three cores and a bin window of 100 years we create a single high-resolution temperature record. The composite record indicates a last glacial (25-19 kyr BP) mixed layer temperature that varies, on average, between 23 and 24 °C (Figure 6C). Starting at 18 kyr BP, the temperature increases gradually, reaching a maximum value of 27°C at 6 kyr BP. Between the mid and late Holocene, mixed layer temperature shows a decrease by about 1°C (Figure 6C).

As described in the method section, we removed the ice volume and calcification temperature effects from the $\delta^{18}O_{G.\ ruber}$ time-series and obtain an estimate of the local $\delta^{18}O$ of mixed layer sea water ($\delta^{18}O_{SW}$) (Figure 6D). A common feature to all three cores is that on orbital-scale the record shows low $\delta^{18}O_{SW}$ values (-0.9‰ to -0.6‰) during the glacial, increasing value during the deglacial, reaching its highest values (0 ‰ to 0.3‰) at about 13-14 kyr BP. During Holocene the $\delta^{18}O_{sw}$ reaches values that vary between -0.2‰ and -0.4‰. Superimposed to the orbital scale trend, the $\delta^{18}O_{SW}$ records reveal multi-centennial scale oscillations. The most prominent of these features are centered between 1 and 4 kyr BP, 11 and 13 kyr BP, 14 and 19 kyr BP, and 23 and 26 kyr BP (Figure 6D) and have relatively low $\delta^{18}Osw$ values.

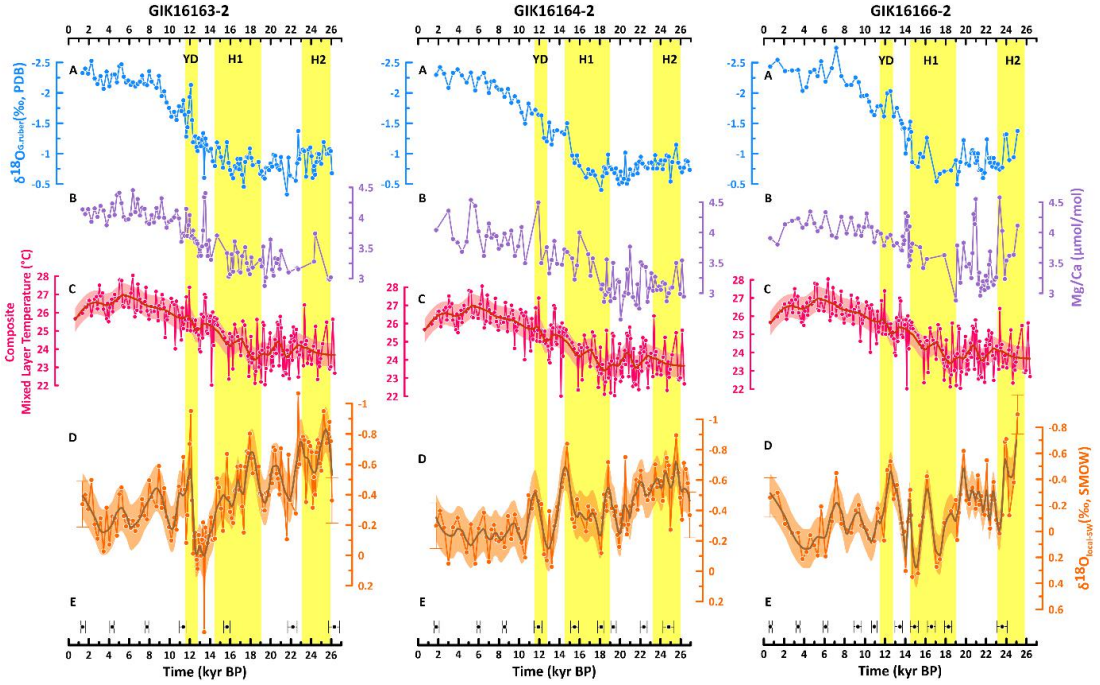

Figure 6: Proxy parameters analyzed in the three marine sediment cores. A and B) $\delta^{18}O$ and Mg/Ca time-series analyzed in test of *G. ruber*. C) Mg/Ca-based mixed layer temperature estimated using a binned (with a 100-year bin window) composite of Mg/Ca data of all three cores, as shown in B. The thick line and envelop indicate a LOESS fit and its 1σ uncertainty. D) local $\delta^{18}O_{sw}$ and E) age model control points and its 2σ uncertainty. Yellow shaded areas indicate episodes of meltwater-induced perturbations of atmospheric and ocean circulation.

5. Discussion

5.1 Regional Hydroclimate

Our interpretation of the local $\delta^{18}O_{sw}$ record is that it harbors a signature of changes in the amount of precipitation changes and isotope composition changes in precipitation over the river basin. Isotope composition changes in precipitation can amplify or weaken the isotope signatures related to changes in the rainfall amount. We hypothesize changes in the amount of precipitation us the dominant factor that shapes the $\delta^{18}O_{sw}$ imprint. Hence, $\delta^{18}O_{sw}$ record provides insights into past hydroclimate changes. Accordingly, the relatively low $\delta^{18}O_{sw}$ values during the last glacial period, recorded in all three sediment cores, indicate a relatively humid period over

northwestern Madagascar because ^{18}O depleted rainfall dilutes the surface water over the core sites. On the orbital scale, the humid glacial episode is followed by a drying trend during the deglacial period (Figures 7A and B). The Holocene varied between dry and moderately humid condition (Figures 7A and B). The orbital scale hydroclimate trend follows the trend of austral summer (DJF) solar insolation over the study region and is broadly consistent with the hydroclimate records of the Zambezi basin (Figures 7D-F) (Schefuß et al., 2011; Wang et al., 2013a; Weldeab et al., 2014). In contrast to our findings, relative to the Holocene drier glacial conditions are suggested for central Madagascar based on a sediment record from Lake Tritrivakely that is located at an elevation of 1778 m (Figures, 1 and 7C) (Williamson et al., 1998). Similarly, a relatively dry condition during the last glacial is indicated in southwestern Madagascar (Scroxton et al., 2019) which is outside the core region of the modern southeastern African monsoon domain (Figures 1 and 7G). Assuming that all proxies are robust indicators of past hydroclimate changes, the temporal and spatial comparison of glacial conditions reveals a north-south gradient and an altitudinal difference, with northern Madagascar being relatively humid and central and southwestern Madagascar relatively dry (Figures 1 and 7) though whether the record from central Madagascar is also representative for the low elevation area remains to be confirmed. Our record of northwestern Madagascar captures glacial hydroclimate imprints that is in line with the records of southern hemisphere monsoon system in Brazil and Australia (Cheng et al., 2016; Cheng et al., 2012; Cruz et al., 2005; Denniston et al., 2013; Strikis et al., 2018; Wang et al., 2007) and contradicts the notion that the monsoonal hydroclimate of Madagascar during the last glacial behaved differently (Williamson et al., 1998). Consistent with the monsoon hypothesis (Kutzbach et al., 2008), the local $\delta^{18}O_{sw}$ record parallels changes in local austral summer insolation (Figure 7A), indicating that strengthening and latitudinal displacement of the ITCZ as the most likely cause for the relatively humid glacial.

On a millennial scale, the $\delta^{18}O_{sw}$ time-series of all three cores exhibit several episodes that are marked by relatively low $\delta^{18}O_{sw}$ values, indicating relatively wet phases. The most prominent features are centered at 11-13, 14-18.5, and 23-26 kyr BP. Taking age model uncertainties up to ±500 years, the timing of the prominent wet phases in northwestern Madagascar coincides with the timing of YD, H1, and H2. This result presents evidence of southeastern African monsoon strengthening in response to meltwater-induced changes in atmospheric circulation.

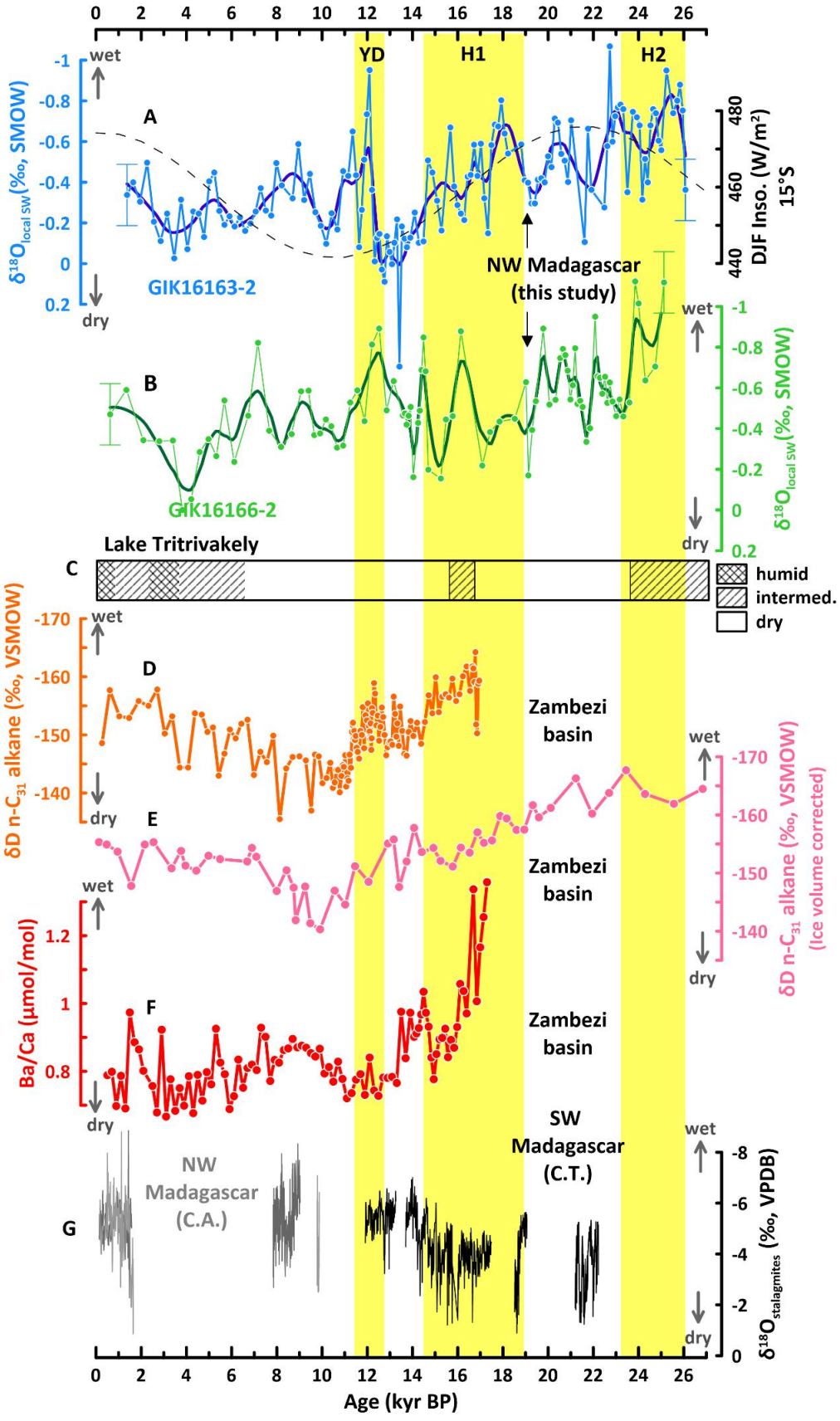
YD
H1
H2
A
B
C
D
E
F
G
wet
dry
GIK16163-2
GIK16166-2
NW Madagascar
(this study)
DJF Inso. (W/m²)
15°S
Lake Tritrivakely
humid
intermed.
dry
Zambezi
basin
SW
Madagascar
(C.T.)
NW
Madagascar
(C.A.)
Age (kyr BP)

Figure 7: Comparison of proxy-based hydroclimate reconstructions over the Madagascar and Zambezi basin (for locations see Figure 1). A and B) $\delta^{18}O_{sw}$ time-series of GIK16163-2 and GIK16163-2 (this study) with fitting curves using LOESS function. Dashed line indicates solar insolation at 15° S during austral summer (December, January & February, DJF) (Laskar et al., 2004). C) Hydroclimate record based on magnetic changes in a sediment core from Lake Tritrivakely (Williamson et al., 1998). D and E) δD n-C_{31} alkane in leaf wax analyzed in off Zambezi marine sediment cores GeoB9307-3 (D) (Schefuß et al., 2011) and GIK16160-3 (E) (Wang et al., 2013a). F) Ba/Ca analyzed in *G. ruber* from marine sediment core GeoB9307-3 and GeoB9310-4 (off Zambezi River) (Weldeab et al., 2014). Yellow shaded areas indicate episodes (YD, H1, and H2) of meltwater-induced perturbations of atmospheric and ocean circulations. G) $\delta^{18}O$ of stalagmites (gray line) from Cave Anjohibe and Anjokipoty in BMMS basin (Voarintsoa et al., 2017) and $\delta^{18}O$ of stalagmites (black line) from Cave Tsimanampesotse located in southern Madagascar (Scroxton et al., 2019). For the duration and timing of H1, the definition of Stanford et al. (2011) was used.

We use the results of climate simulation of Weldeab et al. (2016) to better understand the atmospheric circulation changes and seasonality of precipitation increase over the study area during H1 and YD. The transient simulation data were generated using LOVECLIM, a three-dimensional atmosphere-vegetation-ocean-sea ice-carbon cycle (3x3 resolution) model (Goosse et al., 2010). The control run includes solar insolation and greenhouse gas forcings and the extent of northern hemisphere ice sheet. Freshwater forcing is applied to the North Atlantic region 50°N-70°N to mimic AMOC changes during the H1-Bølling-Allerød (BA)-YD transition (for more details see Weldeab et al. (2016)). In qualitative agreement with the proxy data, the freshwater forced simulation results suggest relatively wet conditions during YD and H1 compared to the control run (Figures 8 and 9). Compared to the austral summer precipitation which shows an intensification and areal expansion relative to the control run (Figure 9), the precipitation increase during the austral winter is weaker (Figure 8) and (relative to the control run) spatially limited (Figures 9), most likely associated with a southward shift of the ITCZ during northern hemisphere monsoon season (austral winter). According to the simulation results, precipitation increase during austral summer was critical to determine the total amount and timing of the annual precipitation increase, especially during H1 (Figures 8B-D).

In contrast to the proxy-based record (Figure 8), the model results suggest a stronger precipitation increase during H1 compared to YD. The difference can possibly be explained by one or a combination of the two scenarios. The model may overestimate the precipitation increase during H1. Alternatively, in addition to isotope changes due to a precipitation amount increase the $\delta^{18}O_{sw}$ record may harbor an imprint of isotope composition changes in precipitation which can be affected by changes in the moisture source and seasonality. Taken together, our proxy record, supported by the climate simulation results, provides strong and consistent evidence

for southern African monsoon intensification in response to meltwater-induced perturbation of atmospheric circulation during the last deglaciation (YD and H2) and the last glacial (H2).

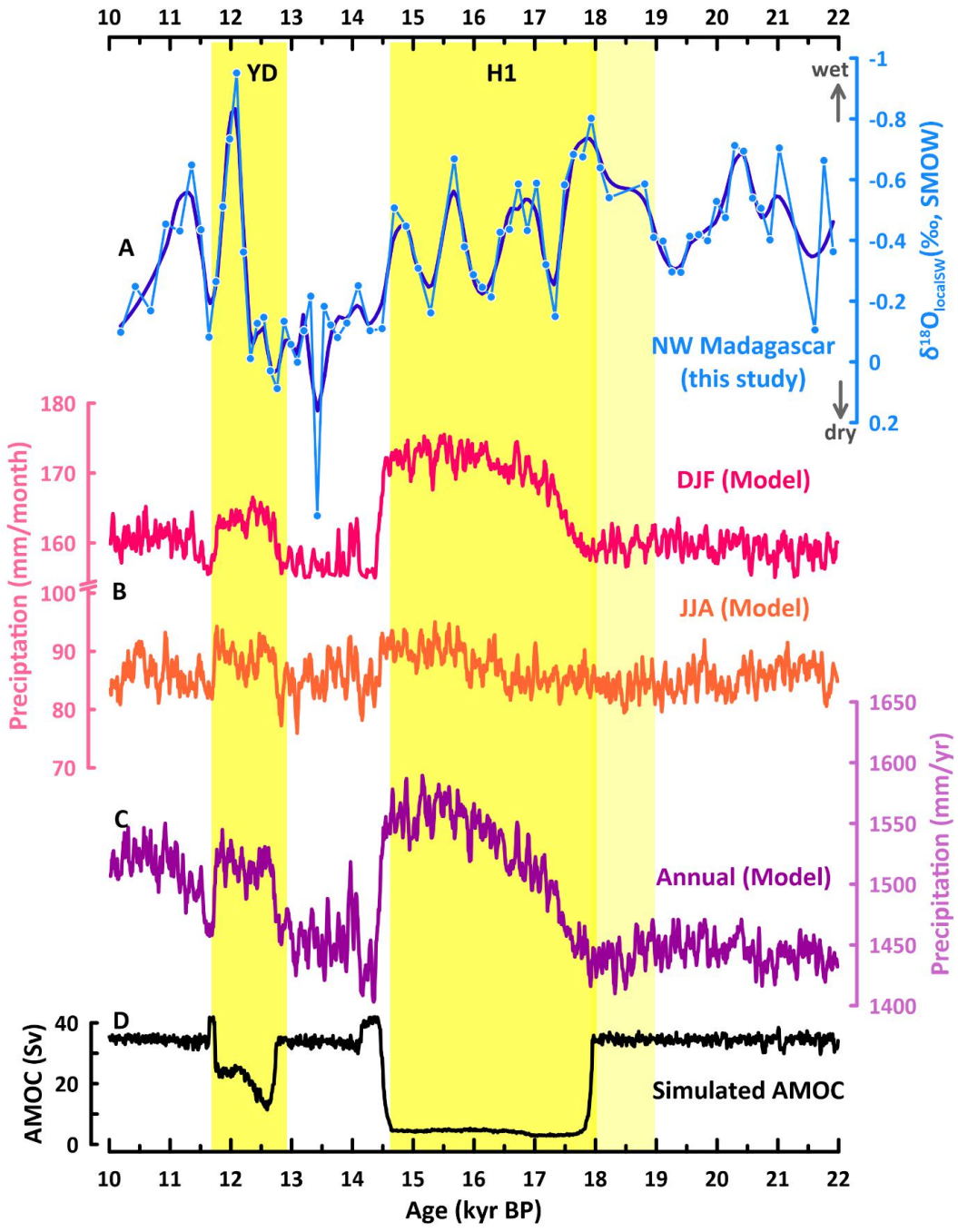

Figure 8: Comparison of simulation- (Weldeab et al., 2016) and proxy-based hydroclimate reconstruction for northwestern Madagascar. A) $\delta^{18}O_{sw}$ time-series analyzed in marine sediment core GIK16163-2 with a fitting curve using LOESS function shown. B) A 10-year average of simulated monthly precipitation (mm/month) over 13.8448°S/50.625°E during austral summer (DJF, pink) and austral winter (JJA, orange). C) A 10-year average of simulated annual

precipitation (mm/year). D) Simulated response of AMOC to freshwater experiments (Weldeab et al., 2016) Yellow shaded areas indicate episodes (YD and H1) of meltwater-induced perturbation of atmospheric and ocean circulations. The combined area shaded with dark and night yellow indicates the timing and duration of H1, as defined by Stanford et al. (2011).

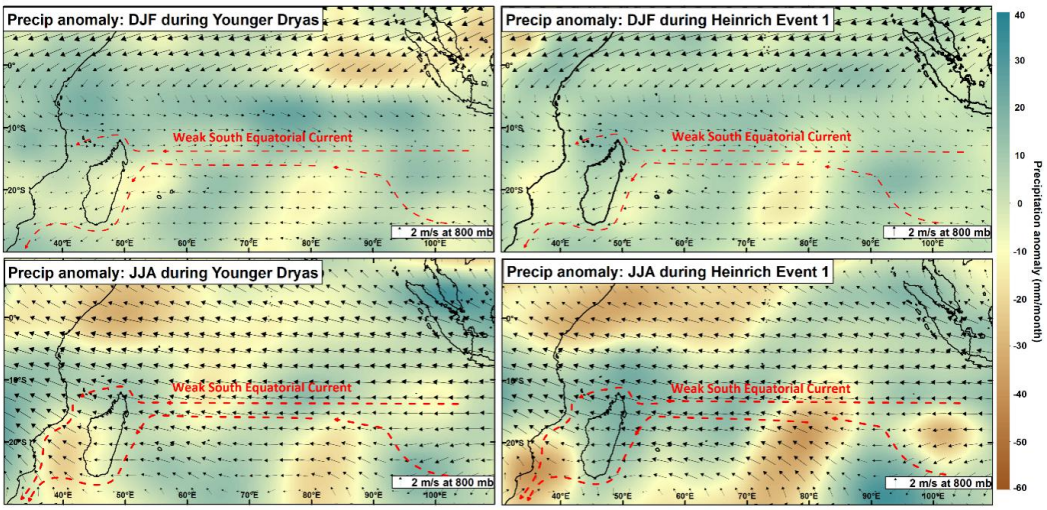

Figure 9: Results of climate (LOVECLIM) simulation (Weldeab et al., 2016), showing seasonal precipitation changes in response to freshwater forcings. Austral summer (top) and austral winter (bottom) precipitation anomaly relative to the control run during YD (left panel) and H1 (right panel): Arrows indicate freshwater experiment results of direction and strength of winds at 800 mbar during YD and H1.

Contrasting our results with other hydroclimate records from central and southeastern Madagascar (Figures 7), it is evident that on millennial-to-centennial scale the climate of Madagascar was temporally and spatially varied with the core region of southern hemisphere monsoon (northwestern Madagascar) experiencing relatively humid conditions during YD, H1, and H2 compared with the rest of the deglaciation and the Holocene period. The lake record from central Madagascar (Figure 7C) indicates dry conditions during the YD episode and wet conditions during H1 and H2 (Williamson et al., 1998), showing a mixed response to the deglacial and glacial meltwater forcings. In contrast to the records from central and northwestern Madagascar, the speleothem record from southwestern tip of Madagascar indicates dry conditions during both YD and H1 relative to the Bølling-Allerørd and the last glacial maximum, respectively (Figure 1G) (Scroxton et al., 2019). Paleohydroclimate studies of the Zambezi Basin show results that are in parts inconsistent, despite applying the same proxy, focusing on the same basin and using marine sediment cores

that were recovered from very close locations (Figures 1, 7D and 7E). The hydrogen isotope time-series analyzed in leaf wax and shown in Figure 7D (Schefuß et al., 2011) indicates humid conditions in the Zambezi basin during the YD and H1 episodes relative to the Bølling-Allerørd and early Holocene. In contrast, the same proxy as in Figure 7D but corrected for global ice volume changes indicates no particular hydroclimate response to the deglacial and glacial freshwater forcings (Figure 7E) (Wang et al., 2013a). A Ba/Ca record analyzed in *G. ruber* and applied as proxy for runoff of the Zambezi River indicates a reduced runoff during the YD relative to the early Holocene and the Bølling-Allerørd (Figure 7F) (Weldeab et al., 2014). Furthermore, the Ba/Ca records suggests dryer conditions in the Zambezi basin during the late phase of H1 relative to the Bølling-Allerørd and early part of H1, an observation that appears to be consistent with the ice volume-corrected hydrogen isotope record (Figure 7E) (Wang et al., 2013a), though the latter is relatively low resolution. Taken together, previous hydroclimate records draw a complex spatio-temporal pattern of millennial-scale past hydroclimate conditions, making it difficult to infer the dominant hydroclimate forcing. The results of our study add to the growing consensus that the southern hemisphere monsoon system was sensitive to and strengthened in response to deglacial and glacial freshwater-induced atmospheric perturbations.

The strengthening of the southern hemisphere monsoon during YD, H1 and H2 in southern Africa, as shown in this study, and studies from South America and Australia (Figure 10) (Cheng et al., 2016; Cheng et al., 2012; Cruz et al., 2005; Denniston et al., 2013; Strikis et al., 2018; Wang et al., 2007) raises the question of a potential climate feedback. An indirect and qualitative measure of past monsoonal wetland expansion linked to the strengthening of all components of southern hemisphere monsoon is an increase in methane release to the atmosphere. While marine hydrates (Kennett et al., 2003) and land permafrost (Winterfeld et al., 2018) can contribute to an increase of atmospheric methane, results of carbon and hydrogen isotope analyses in atmospheric methane indicate that the dominant sources of glacial and deglacial atmospheric methane were tropical wetlands and floodplains (Bock et al., 2017; Dyonisius et al., 2020). Indeed, allowing for age model uncertainties in the atmospheric methane and precipitation proxy records, the southern hemisphere monsoon strengthening during YD, H1 and H2 coincides or overlaps with moderate increases in atmospheric methane (Figure 10, right column). The YD is punctuated by several episodes of atmospheric methane increase in the range of 41 ppb. The interval of H1 is marked by a gradual increase of atmospheric methane from ~380 ppb at 18 kyr BP to 480 ppb at 14.5 kyr BP. Overlapping with the timing of H2, atmospheric methane increased abruptly from 360 ppb to 400 ppb (Figure 10, right column). Since the northern

hemisphere monsoon system was weak (Cheng et al., 2016; Cheng et al., 2012; Wang et al., 2001; Weldeab et al., 2007), it is most likely that the atmospheric methane increase during YD, H1 and H2 is associated with southern hemisphere monsoon strengthening, potentially providing an important feedback mechanism between a potent greenhouse gas and southern hemispheric tropical hydroclimate changes in response to meltwater forcings. Added to the increase of atmospheric CO_2 during YD and Heinrich events (Ahn and Brook, 2008; Luthi et al., 2008), the moderate increases of atmospheric methane most likely contributed to the tropical ocean warmings that parallel that the timings of Heinrich events (Weldeab, 2012).

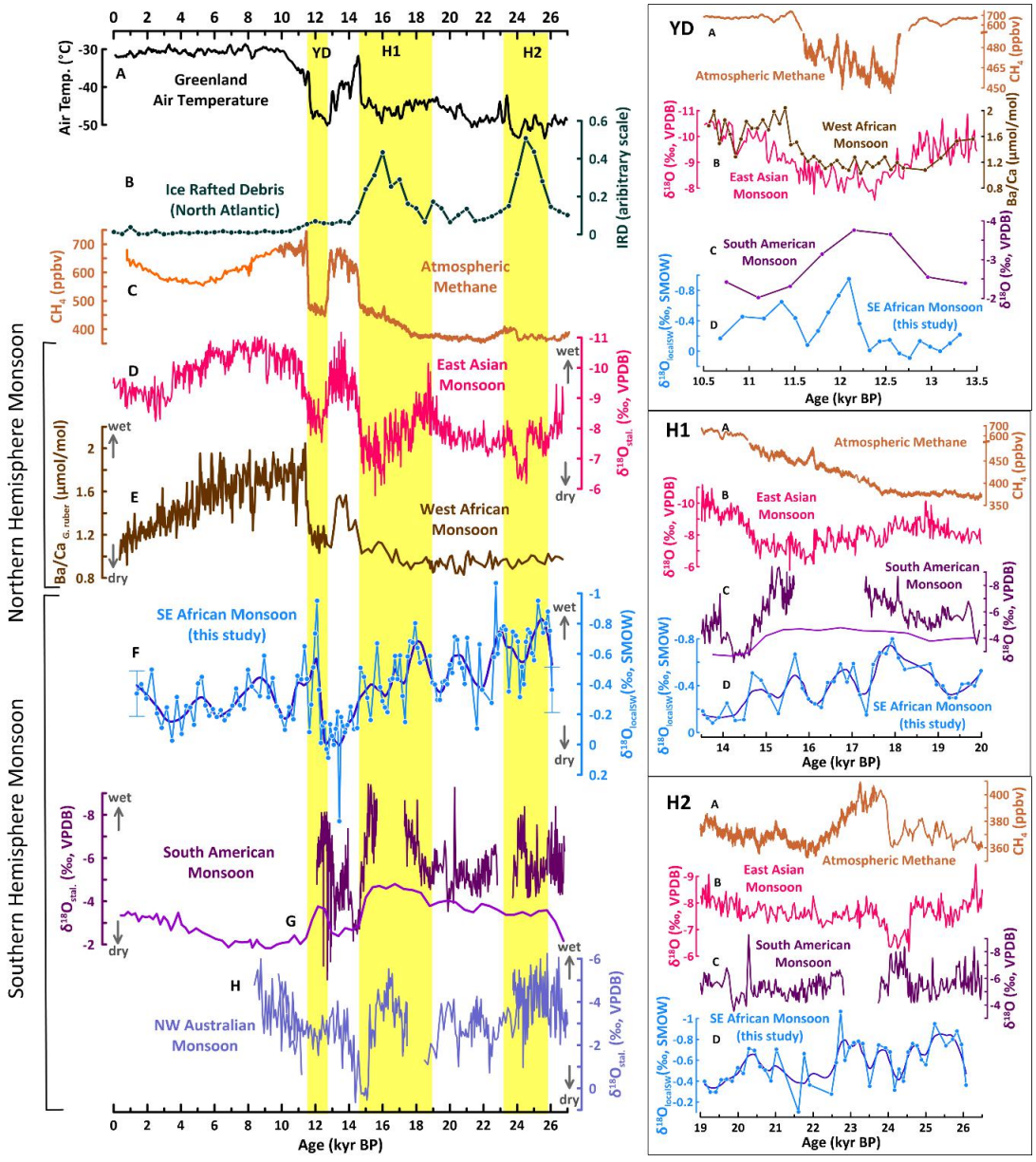

Figure 10: Millennial-scale northern high climate changes and associated response of northern hemisphere and southern hemisphere monsoon systems. Left panel: A) Air temperature changes over Greenland (Alley, 2000). B) ice rafted debris (IRD) compiled from several North Atlantic marine sediment records (Stern and Lisiecki, 2013). C) Atmospheric methane concentration analyzed in Antarctica ice cores (orange: Spahni et al. (2005), brown: Rhodes et al. (2017). D) $\delta^{18}O$ of stalagmites from Dongge Cave in China (Cheng et al., 2016) as proxy of East Asian monsoon. E) Ba/Ca in *G.ruber* from a Gulf of Guinea sediment core as a proxy for West African monsoon. F) $\delta^{18}O_{sw}$ of core GIK16163-2 (this study) with a fitting curve using LOESS function. E) $\delta^{18}O$ of stalagmites from Botuverá Cave in Brazil (Wang et al., 2007) and Lapa Sem Fim Cave in Brazil Strikis et al. (2018) as a proxy for South American monsoon changes. G) $\delta^{18}O$ of stalagmites from northern Australia (Denniston et al., 2013). Right panel: Close views of selected southern and northern monsoon proxy records and atmospheric methane record during YD (top panel), H1 (middle panel), and H2 (bottom panel).

5.2 SST gradient changes within the Mozambique Channel and reduced throughflow

The long-term trend of our mixed layer temperature reconstruction shows a gradual increase by 2.5-3 °C between the early deglacial (18 kyr BP) and the middle Holocene (4 kyr BP). The temperature trend during the glacial and deglaciation largely parallels the trend of atmospheric CO_2 and air temperature over Antarctica (Figure 11). With a gradual increase between the early and mid-Holocene and a decline between the mid and late Holocene by about one degree, the Holocene mixed layer temperature most likely indicates a signature of regional and global forcings. The east-west gradient of mixed layer temperature within Mozambique Channel is controlled by wind fields and the wind-driven South Equatorial Current of the tropical Indian Ocean that drives Mozambique Channel throughflow (Figures 1 and 3) (Backeberg and Reason, 2010). The latter propagates along the African continental margin and contributes to the manifestation of colder SSTs than in the eastern Mozambique Channel. Hence, past spatial variation of mixed layer temperature within the Mozambique Channel provides crucial insights about changes in wind-driven water mass transport through the channel.

We use the Mg/Ca-based SST record of western Mozambique Channel (Wang et al., 2013b) and our composite SST record of eastern Mozambique Channel to create a time-series of west-east SST gradient reconstruction (Figure 11). Given the relatively large uncertainty of Mg/Ca-based SST reconstruction (1σ: ±0.65°C), our focus is on

long-term trends and average values over extended intervals. SST gradient during the Holocene (0-10.5 kyr BP) shows a negative gradient with an average value of -1.3 °C, indicating that the current thermal gradient between the eastern and western Mozambique Channel was established since the early Holocene. During the last glacial period, the temperature gradient is weak relative to that of the Holocene. The most outstanding feature of the spatio-temporal temperature reconstruction is a gradient reversal between 14.5 and 19 kyr BP, showing a warmer western than the eastern Mozambique Channel. The timing and duration of the temperature gradient reversal coincided, within age model uncertainties, with the timing of the meltwater-induced AMOC weakening during H1, increase of atmospheric CO_2, warming of tropical oceans and air temperature rise over Antartica (Figure 11). We suggest that this fundamental change in the thermal structure of the Mozambique Channel is linked to a large-scale change in the wind field over the tropical Indian Ocean and, as result, water mass transport through the Mozambique Channel that influences the heat and salt exchanges between the tropical Indian Ocean and the Atlantic. Our association of wind field and temperature gradient changes in the Mozambique Channel is consistent the results of the hosing experiment that, relative to the modern conditions (Figure 1), indicate a weakening of the wind field and westward shift of the wind direction in austral winter during H1 and YD (Figure 9). The changes in the wind direction over tropical Indian Ocean during H1 and YD, as indicated by the model results, weakens the westward/zonal Ekman transport (South Equatorial Current) across the tropical Indian Ocean and reduces the Mozambique Channel throughflow that is a key component of the Agulhas Current. Noting that the Agulhas leakage is controlled by the latitude of maximum (southern hemisphere) westerlies and the position and strength of wind fields over the Indian Ocean, we hypothesize that the reduced Mozambique Channel throughflow, as suggested by our study, weakens the Agulhas Current and Agulhas leakage during H1.

Previous studies, based on records mostly from sites south of South Africa, suggest a strengthening of Agulhas leakage during deglaciations (Beal et al., 2011; Caley et al., 2012; Franzese et al., 2006; Peeters et al., 2004; Simon et al., 2013). A close look at the millennial-scale segments of the records, though complicated by the low resolution of the time-series, reveals that during Heinrich events the Agulhas leakage proxy draws a complex and temporally inconsistent picture, with some Heinrich episodes accompanied by a reduced Agulhas leakage and others by an increased Agulhas leakage (Simon et al., 2013). It has been noted that reconstruction sites within the Indian Ocean sector of the Agulhas Current may also harbor signatures of Agulhas Return Current (Simon et al., 2013).

We compare our results with the results of Peeters et al. (2004) in the Cape Basin

(Atlantic sector), west of the retroflection and the shedding region, that is most likely to capture changes in the Agulhas leakage (Figure 1B). In agreement with our result and conclusion, the foraminiferal assemblage-based reconstruction (Peeters et al., 2004) indicates a reduced Agulhas leakage during H1, though the resolution is relatively low (Figure 11G). Satellite data and modeling studies reveal that due to the warming climate the Subtropical Front and the latitude of maximum westerlies are shifting southward, allowing enhanced Agulhas leakage (Backeberg et al., 2012; Biastoch and Boning, 2013; Biastoch et al., 2008; Biastoch et al., 2009; Biastoch et al., 2015). Similarly, parallel to the rise of air temperature over Antarctica, warming of the Southern Ocean, and atmospheric CO_2 concentration increase (Figure 11), model- and proxy-based reconstructions suggest a southward shift of the Subtropical Front and the southern hemisphere westerlies during H1 (Anderson et al., 2009; Shemesh et al., 2002; Toggweiler et al., 2006). A weakened Agulhas leakage, as suggested in (Peeters et al., 2004), at the time of southward shifted westerlies (Anderson et al., 2009; Shemesh et al., 2002; Toggweiler et al., 2006) is inconsistent with the notion of position shift of the westerlies as the most dominant factor that controls Agulhas leakage. We hypothesize that changes in the strength and direction of trade winds over the tropical Indian Ocean during H1 weakened the Agulhas Current and reduced the Agulhas leakage. The broader implication of the changes in the tropical Indian Ocean wind field in response to freshwater-induced perturbation is creating a positive feedback that potentially contributes to sustaining the weakened AMOC during Heinrich events by reducing the amount of salt leakage into the Atlantic.

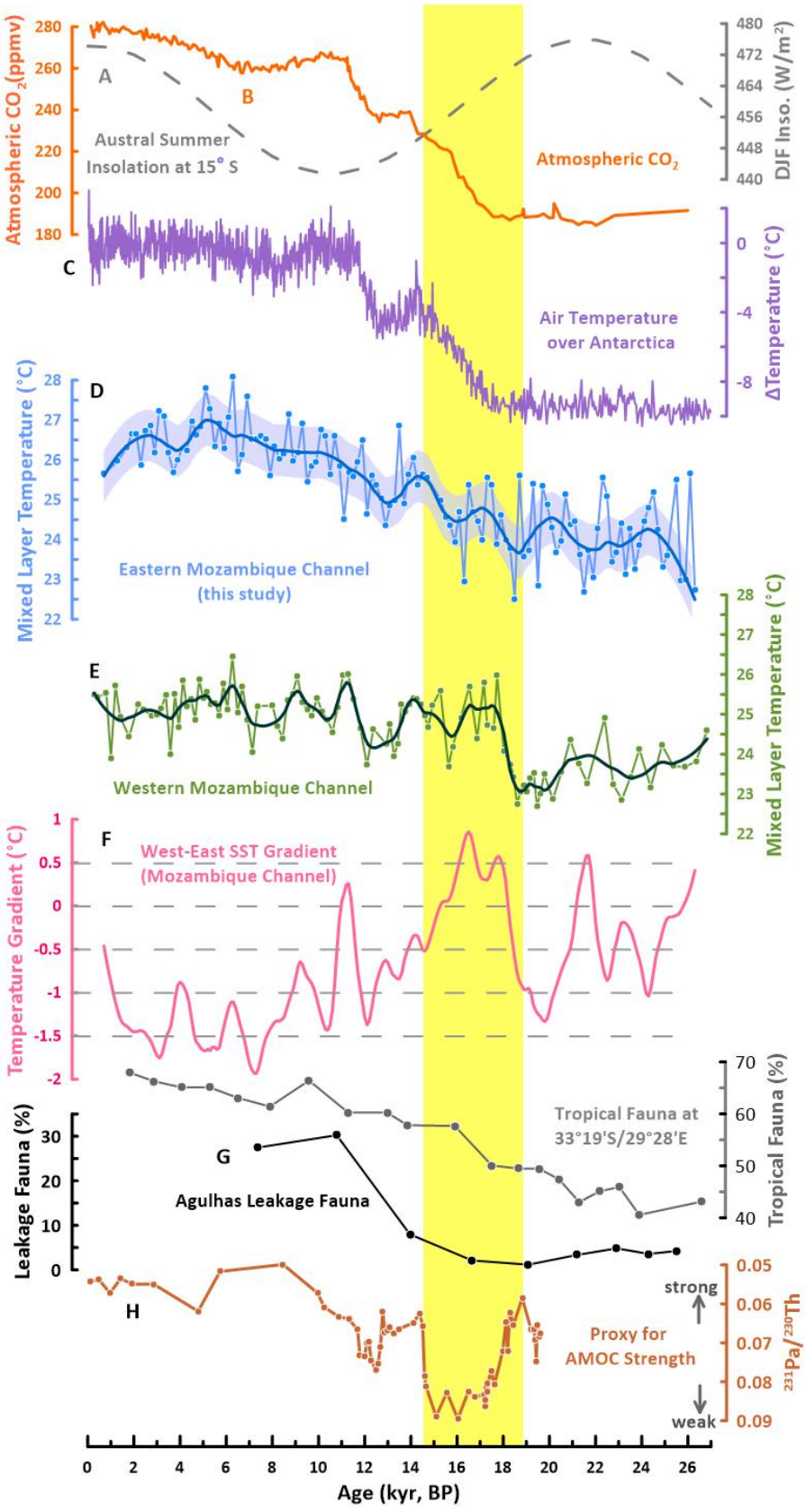
Atmospheric CO2(ppmv)
280
260
240
220
200
180
A
B
Austral Summer
Insolation at 15° S
Atmospheric CO2
480
472
464
456
448
440
DJF Inso. (W/m2)
C
Air Temperature
over Antarctica
0
-4
-8
ΔTemperature (°C)
Mixed Layer Temperature (°C)
28
27
26
25
24
23
22
D
Eastern Mozambique Channel
(this study)
E
Western Mozambique Channel
Mixed Layer Temperature (°C)
Temperature Gradient (°C)
1
0.5
0
-0.5
-1
-1.5
-2
F
West-East SST Gradient
(Mozambique Channel)
Tropical Fauna at
33°19'S/29°28'E
70
60
50
40
Tropical Fauna (%)
Leakage Fauna (%)
30
20
10
0
G
Agulhas Leakage Fauna
H
strong
Proxy for
AMOC Strength
weak
0.05
0.06
0.07
0.08
0.09
231Pa/230Th
0
2
4
6
8
10
12
14
16
18
20
22
24
26
Age (kyr, BP)

Figure 11: Mixed layer temperature changes within Mozambique Channel and climate forcings. A) Austral summer solar insolation at 15° S (Laskar et al., 2004). B) Atmospheric CO_2 concentration analyzed in Antarctica ice cores (Luthi et al., 2008). C) Changes in air temperature over Antarctica (Dom C) relative to the year 1950 (Jouzel et al., 2007). D) Mg/Ca-based composite mixed layer temperature record in eastern Mozambique Channel (this study). E) Mg/Ca-based mixed layer temperature record in western Mozambique Channel (Wang et al., 2013b). F) West-east SST gradient within Mozambique Channel calculated using temperature time-series shown in Figure 11C and 11D. G) Agulhas leakage fauna in percentage (Peeters et al., 2004). H) $^{231}Pa/^{230}Th$ analyzed in a North Atlantic sediment core and used as a proxy for relative changes in AMOC (McManus et al., 2004). Yellow shaded area indicates the time period of positive west-east SST gradient, and grey shaded area indicates the time period with a weak west-east SST gradient.

6. Summary and Conclusion

We generated a 26,000 year-long hydroclimate and thermal record based on the analysis of three marine sediment cores recovered from eastern Mozambique, off northwestern Madagascar. Our study indicates that northwestern Madagascar was relatively humid during the last glacial and during millennial-scale periods of YD, H1, and H2. This finding highlights the sensitivity of the southern African monsoon to freshwater-induced changes in atmospheric circulation. The southern hemisphere monsoonal strengthening and associated expansion of wetlands and floodplains during Heinrich events provide a viable explanation for the moderate increase of atmospheric methane, a potent greenhouse gas, presenting a potential positive climate feedback.

The long-term trend and magnitude of change in our high-resolution Mg/Ca-based temperature record is largely dominated by changes in atmospheric CO_2. Contrasting temperature record from off the Zambezi River and off northwestern Madagascar reveals a reversal in the west-east gradient during H1, indicating a fundamental thermal reorganization associated with a weakening of the wind-driven Southern Equatorial Current and, as a result, a weakening of water mass transport through the Mozambique Channel. This implies that independent from shifts of the southern westerlies, changes in the wind field over the tropical Indian Ocean exerts an important control on the Agulhas Current and Agulhas leakage variability that is thought to affect the AMOC. Sensitivity of the wind-driven Southern Equatorial Current and Mozambique Channel throughflow to meltwater-induced perturbations of northern high latitude climate potentially presents a feedback mechanism that

contributes to sustaining a weakened AMOC during Heinrich events.

.

7. Cited References

Adkins, J.F., et al., 2002. The Salinity, Temperature, and delta 18O of the Glacial Deep Ocean. Science 298, 1769-1773.

Ahn, J., Brook, E.J., 2008. Atmospheric CO2 and Climate on Millennial Time Scales During the Last Glacial Period. Science 322, 83-85.

Alley, R.B., 2000. The Younger Dryas cold interval as viewed from central Greenland. Quaternary Science Review 19, 213-226.

Anderson, R.F., et al., 2009. Wind-Driven Upwelling in the Southern Ocean and the Deglacial Rise in Atmospheric CO2. Science 323, 1443-1448.

Arivelo, T.A., Lin, Y.-L., 2016. Climatology of Heavy Orographic Rainfall Induced by Tropical Cyclones over Madagascar: From Synoptic to Mesoscale Perspectives. Earth Science Research 5, 132-147.

Backeberg, B.C., et al., 2012. Impact of intensified Indian Ocean winds on mesoscale variability in the Agulhas system. Nature Climate Change 2, 608-612.

Backeberg, B.C., Reason, C.J.C., 2010. A connection between the South Equatorial Current north of Madagascar and Mozambique Channel Eddies. Geophysical Research Letters 37, 10.1029/2009GL041950.

Beal, L.M., et al., 2011. On the role of the Agulhas system in ocean circulation and climate. Nature 472, 429-436.

Behringer, D.W., Xue, Y., 2004. Evaluation of the global ocean data assimilation system at NCEP: The Pacific Ocean. Eighth Symposium on Integrated Observing and Assimilation Systems for Atmosphere, Oceans, and Land Surface AMS 84th Annual Meeting, Washington State Convention and Trade Center, Seattle, Washington, 11-15.

Bemis, B.E., et al., 1998. Reevaluation of oxygen isotope composition of planktonic foraminifera: experimental results and revised paleotemperature equations. Paleoceanography 13, 150-160.

Biastoch, A., Boning, C.W., 2013. Anthropogenic impact on Agulhas leakage. Geophysical Research Letters 40, 1138-1143.

Biastoch, A., et al., 2008. Agulhas leakage dynamics affects decadal variability in Atlantic overturning circulation. Nature 456, 489-492.

Biastoch, A., et al., 2009. Increase in Agulhas leakage due to poleward shift of Southern Hemisphere westerlies. Nature 462, 495-498.

Biastoch, A., et al., 2015. Atlantic multi-decadal oscillation covaries with Agulhas leakage. Nat Commun 6, 10.1038/ncomms10082.

Biastoch, A., et al., 1999. The importance of flow in the Mozambique Channel to seasonality in the greater Agulhas Current System. Geophysical Research Letters 26,

3321-3324.
Blaauw, M., Christen, J.A., 2011. Flexible Paleoclimate Age-Depth Models Using an Autoregressive Gamma Process. Bayesian Analysis 6, 457-474.
Bock, M., et al., 2017. Glacial/interglacial wetland, biomass burning, and geologic methane emissions constrained by dual stable isotopic CH4 ice core records. Proceedings of the National Academy of Sciences of the United States of America 114, E5778-E5786.
Bowen, G.J., et al., 2005. Global application of stable hydrogen and oxygen isotopes to wildlife forensics. Oecologia 143, 337-348.
Bryden, H.L., et al., 2005. Structure and transport of the Agulhas Current and its temporal variability. J Oceanogr 61, 479-492.
Caley, T., et al., 2012. Agulhas leakage as a key process in the modes of Quaternary climate changes. Proceedings of the National Academy of Sciences 109, 6835-6839.
Cheng, H., et al., 2016. The Asian monsoon over the past 640,000 years and ice age terminations. Nature 534, 640-646.
Cheng, H., et al., 2012. The Global Paleomonsoon as seen through speleothem records from Asia and the Americas. Climate Dynamics 39, 1045-1062.
Cruz, F.W., et al., 2005. Insolation-driven changes in atmospheric circulation over the past 116,000 years in subtropical Brazil. Nature 434, 63-66.
Denniston, R.F., et al., 2013. North Atlantic forcing of millennial-scale Indo-Australian monsoon dynamics during the Last Glacial period. Quaternary Science Reviews 72, 159-168.
Dyonisius, M.N., et al., 2020. Old carbon reservoirs were not important in the deglacial methane budget. Science 367, 907-+.
Franzese, A.M., et al., 2006. Reduced Agulhas Leakage during the Last Glacial Maximum inferred from an integrated provenance and flux study. Earth and Planetary Science Letters 250, 72-88.
Goosse, H., et al., 2010. Description of the Earth system model of intermediate complexity LOVECLIM version 1.2. Geosci Model Dev 3, 603-633.
Gray, W.R., Evans, D., 2019. Nonthermal Influences on Mg/Ca in Planktonic Foraminifera: A Review of Culture Studies and Application to the Last Glacial Maximum. Paleoceanography and Paleoclimatology 34, 306-315.
Gray, W.R., et al., 2018. The effects of temperature, salinity, and the carbonate system on Mg/Ca in Globigerinoides ruber (white): A global sediment trap calibration. Earth and Planetary Science Letters 482, 607-620.
Greaves, M., et al., 2008. Interlaboratory comparison study of calibration standards for foraminiferal Mg/Ca thermometry. Geochem Geophy Geosy 9, 10.1029/2008gc001974.
Han, G., et al., 2019. SST Anomalies in the Mozambique Channel Using Remote Sensing and Numerical Modeling Data. Remote Sensing 11, 1112.
Huffman, G.J., et al., 2019. GPM IMERG Final Precipitation L3 1 month 0.1 degree x 0.1 degree V05, Greenbelt, MD, Goddard Earth Sciences Data and Information

Services Center (GES DISC), accessed [2019/10/30], 10.5067/GPM/IMERG/3B-MONTH/06.
Jouzel, J., et al., 2007. Orbital and millennial Antarctic climate variability over the past 800,000 years. Science 317, 793-796.
Kalnay, E., et al., 1996. The NCEP/NCAR 40-year reanalysis project. Bulletin of the American Meteorological Society 77, 437-471.
Kennett, J.P., et al., 2003. Methane Hydrates in Quaternary Climate Change. American Geophysical Union, Washington, DC.
Khon, V.C., et al., 2014. Climate and CO2 effects on the vegetation of southern tropical Africa over the last 37,000 years. Earth and Planetary Science Letters 403, 407-417.
Kutzbach, J.E., et al., 2008. Simulation of the evolutionary response of global summer monsoons to orbital forcing over the past 280,000 years. Climate Dynamics 30, 567-579.
Lambeck, K., et al., 2014. Sea level and global ice volumes from the Last Glacial Maximum to the Holocene. Proceedings of the National Academy of Sciences 111, 15296-15303.
Laskar, J., et al., 2004. A long-term numerical solution for the insolation quantities of the Earth. Astronomy and Astrophysics 428, 261-285.
Lee, K., et al., 2006. Global relationships of total alkalinity with salinity and temperature in surface waters of the world's oceans. Geophysical Research Letters 33, 10.1029/2006gl027207.
Locarnini, R.A., et al., 2013. World Ocean Atlas 2013, Volume 1: Temperature. S. Levitus, Ed., A. Mishonov Technical Ed.; NOAA Atlas NESDIS 73, 40 pp.
Lougheed, B.C., Obrochta, S.P., 2019. A Rapid, Deterministic Age-Depth Modeling Routine for Geological Sequences With Inherent Depth Uncertainty. Paleoceanography and Paleoclimatology 34, 122-133.
Luthi, D., et al., 2008. High-resolution carbon dioxide concentration record 650,000-800,000 years before present. Nature 453, 379-382.
Malauene, B.S., et al., 2014. Cool, elevated chlorophyll-a waters off northern Mozambique. Deep Sea Research Part II: Topical Studies in Oceanography 100, 68-78.
Marino, G., et al., 2013. Agulhas salt-leakage oscillations during abrupt climate changes of the Late Pleistocene. Paleoceanography, n/a-n/a.
Martin, P.A., Lea, D.W., 2002. A simple evaluation of cleaning procedures on fossil benthic foraminiferal Mg/Ca. Geochem Geophy Geosy 3, 10.1029/2001GC000280.
Martinez-Mendez, G., et al., 2010. Contrasting multiproxy reconstructions of surface ocean hydrography in the Agulhas Corridor and implications for the Agulhas Leakage during the last 345,000 years. Paleoceanography 25.
Marwick, T.R., et al., 2014. Disproportionate Contribution of Riparian Inputs to Organic Carbon Pools in Freshwater Systems. Ecosystems 17, 974-989.
McManus, J.F., et al., 2004. Collapse and rapid resumption of Atlantic meridional

circulation linked to deglacial climate changes. Nature 428, 834-837.
Peeters, F.J.C., et al., 2004. Vigorous exchange between the Indian and Atlantic oceans at the end of the past five glacial periods. Nature 430, 661-665.
Reimer, P.J., et al., 2013. IntCal13 and Marine13 Radiocarbon Age Calibration Curves 0–50,000 Years cal BP. Radiocarbon 55, 1869-1887.
Rhodes, R.H., et al., 2017. Atmospheric methane variability: Centennial-scale signals in the Last Glacial Period. Global Biogeochem Cy 31, 575-590.
Richardson, P.L., 2007. Agulhas leakage into the Atlantic estimated with subsurface floats and surface drifters. Deep-Sea Res Pt I 54, 1361-1389.
Ridderinkhof, H., de Ruijter, W.P.M., 2003. Moored current observations in the Mozambique Channel. Deep-Sea Res Pt Ii 50, 1933-1955.
Ridderinkhof, H., et al., 2010. Seasonal and interannual variability in the Mozambique Channel from moored current observations. Journal of Geophysical Research 115, 10.1029/2009jc005619.
Ryan, W.B.F., et al., 2009. Global Multi-Resolution Topography synthesis. Geochem Geophy Geosy 10, 10.1029/2008GC002332.
Schefuß, E., et al., 2011. Forcing of wet phases in southeast Africa over the past 17,000 years. Nature 480, 509-512.
Schiebel, R., Hemleben, C., 2017. Planktonic foraminifers in the modern ocean. Springer, Berlin, Heidelberg.
Schneider, R.R., et al., 2008. Western Indian Ocean Climate and Sedimentation – WINOCS SAMBESI II
Schott, F.A., et al., 2009. Indian Ocean Circulation and Climate Variability. Reviews of Geophysics 47, 10.1029/2007RG000245.
Scroxton, N., et al., 2019. Competing Temperature and Atmospheric Circulation Effects on Southwest Madagascan Rainfall During the Last Deglaciation. Paleoceanography and Paleoclimatology 34, 275-286.
Shemesh, A., et al., 2002. Sequence of events during the last deglaciation in Southern Ocean sediments and Antarctic ice cores. Paleoceanography 17.
Simon, M.H., et al., 2013. Millennial-scale Agulhas Current variability and its implications for salt-leakage through the Indian–Atlantic Ocean Gateway. Earth and Planetary Science Letters 383, 101-112.
Southon, J., et al., 2002. Marine reservoir corrections for the Indian Ocean and Southeast Asia. Radiocarbon 44, 167-180.
Spahni, R., et al., 2005. Atmospheric methane and nitrous oxide of the late Pleistocene from Antarctic ice cores. Science 310, 1317-1321.
Spratt, R.M., Lisiecki, L.E., 2016. A Late Pleistocene sea level stack. Climate of the Past 12, 1079-1092.
Stanford, J.D., et al., 2011. A new concept for the paleoceanographic evolution of Heinrich event 1 in the North Atlantic. Quaternary Science Reviews 30, 1047-1066.
Stern, J.V., Lisiecki, L.E., 2013. North Atlantic circulation and reservoir age changes over the past 41,000years. Geophysical Research Letters 40, 3693-3697.

Strikis, N.M., et al., 2018. South American monsoon response to iceberg discharge in the North Atlantic. Proceedings of the National Academy of Sciences of the United States of America 115, 3788-3793.
Stuiver, M., et al., 2019. CALIB 7.1. [WWW program] at http://calib.org, accessed [2019/1/24].
Swart, N.C., et al., 2010. Observed characteristics of Mozambique Channel eddies. Journal of Geophysical Research 115, 10.1029/2009jc005875.
Toggweiler, J.R., et al., 2006. Midlatitude westerlies, atmospheric CO2, and climate change during the ice ages. Paleoceanography 21.
U.S. Geological Survey's Center for Earth Resources Observation and Science, E., 1996. 30 arc-second DEM of Africa.
van der Werf, P.M., et al., 2010. Comparison between observations and models of the Mozambique Channel transport: Seasonal cycle and eddy frequencies. Journal of Geophysical Research 115, 10.1029/2009jc005633.
Voarintsoa, N.R.G., et al., 2017. Three distinct Holocene intervals of stalagmite deposition and nondeposition revealed in NW Madagascar, and their paleoclimate implications. Climate of the Past 13, 1771-1790.
von der Heydt, A., Dijkstra, H.A., 2008. The effect of gateways on ocean circulation patterns in the Cenozoic. Global and Planetary Change 62, 132-146.
Waelbroeck, C., et al., 2002. Sea-level and deep water temperature changes derived from benthic foraminifera isotopic records. Quaternary Science Research 21, 295-305.
Wang, X., et al., 2007. Millennial-scale precipitation changes in southern Brazil over the past 90,000 years. Geophysical Research Letters 34, 10.1029/2007gl031149.
Wang, Y., et al., 2001. A high-resolution absolute-dated Late Pleistocene monsoon record from Hulu Cave, China. Science 294, 2345-2348.
Wang, Y.V., et al., 2013a. What does leaf wax δD from a mixed C3/C4 vegetation region tell us? Geochimica et Cosmochimica Acta 111, 128-139.
Wang, Y.V., et al., 2013b. Northern and southern hemisphere controls on seasonal sea surface temperatures in the Indian Ocean during the last deglaciation. Paleoceanography 28, 619-632.
Weldeab, S., 2012. Timing and magnitude of equatorial Atlantic surface warming during the last glacial bipolar oscillation. Climate of the Past 8, 1705-1716.
Weldeab, S., et al., 2016. Strong middepth warming and weak radiocarbon imprints in the equatorial Atlantic during Heinrich 1 and Younger Dryas. Paleoceanography 31, 1070-1082.
Weldeab, S., et al., 2014. Links between southwestern tropical Indian Ocean SST and precipitation over southeastern Africa over the last 17kyr. Palaeogeography, Palaeoclimatology, Palaeoecology 410, 200-212.
Weldeab, S., et al., 2007. 155,000 years of West African monsoon and ocean thermal evolution. Science 316, 1303-1307.
Wentz, F., et al., 2014. Aquarius Level 3 Sea Surface Salinity Standard Mapped Image Annual Data V3.0. Ver. 3.0. PO.DAAC, CA, USA. Dataset accessed [2019/10/30] at

https://doi.org/10.5067/AQUAR-3SAPS.
Williamson, D., et al., 1998. Mineral-magnetic proxies of erosion/oxidation cycles in tropical maar-lake sediments (Lake Tritrivakely, Madagascar): paleoenvironmental implications. Earth and Planetary Science Letters 155, 205-219.
Winterfeld, M., et al., 2018. Deglacial mobilization of pre-aged terrestrial carbon from degrading permafrost. Nature Communications 9.
Zweng, M.M., et al., 2013. World Ocean Atlas 2013, Volume 2: Salinity. S. Levitus, Ed., A. Mishonov Technical Ed.; NOAA Atlas NESDIS 74, 39 pp.